

# A Third-order Compact Gas-kinetic Scheme on Unstructured Meshes for Compressible Navier-Stokes Solutions

Liang Pan<sup>a</sup>, Kun Xu<sup>a,b,\*</sup>

<sup>a</sup>*Department of Mathematics, Hong Kong University of Science and Technology, Clear Water Bay, Kowloon, Hong Kong*

<sup>b</sup>*Department of Mechanical and Aerospace Engineering, Hong Kong University of Science and Technology, Clear Water Bay, Kowloon, Hong Kong*

---

## Abstract

In this paper, for the first time a compact third-order gas-kinetic scheme is proposed on unstructured meshes for the compressible viscous flow computations. The possibility to design such a third-order compact scheme is due to the high-order gas evolution model, where a time-dependent gas distribution function at a cell interface not only provides the fluxes across a cell interface, but also the time evolution of the flow variables at the cell interface as well. As a result, both cell averaged and cell interface flow variables can be used for the initial data reconstruction at the beginning of next time step. A weighted least-square reconstruction has been used for the construction of a third-order initial condition. Therefore, a compact third-order gas-kinetic scheme with the involvement of neighboring cells only can be developed on unstructured meshes. In comparison with other conventional high-order schemes, the current method avoids the use of Gaussian points for the flux integration along a cell interface and the multi-stage Runge-Kutta time stepping technique. The third-order compact scheme is numerically stable under CFL condition above 0.5. Due to the multidimensional gas-kinetic formulation and the coupling of inviscid and viscous terms, even with unstructured meshes the boundary layer solution and the vortex structure can be accurately captured in the current scheme. At the same time, the compact scheme can capture strong shocks as well.

**Keywords:** high-order scheme, gas-kinetic scheme, compact reconstruction, unstructured mesh, weighted least-square reconstruction.

---

## 1. Introduction

In computational fluid dynamics, the second-order methods are generally robust and reliable, and they are routinely employed in the practical calculations. For the same computational cost, higher-order methods can provide more accurate solutions, but they are less

---

\*Corresponding author

Email addresses: panliangjlu@sina.com (Liang Pan), makxu@ust.hk (Kun Xu)

robust and more complicated. In recent decades, there has been a continuous interesting and effort on the development of higher-order schemes. For engineering applications, the construction of higher-order numerical schemes on unstructured meshes becomes extremely demanding. Since a gigantic amount of publications have been devoted to the introduction and survey of higher-orders schemes, the current paper will mainly concentrate on the construction of the third-order compact gas-kinetic scheme on unstructured meshes.

The gas-kinetic scheme (GKS) has been developed systematically for the compressible flow computations [23, 24, 14, 10]. An evolution process from kinetic to hydrodynamic scales has been constructed for the flux evaluation. The kinetic effect through particle free transport contributes to the capturing of the shock wave, and the hydrodynamic effect plays a dominant role for the resolved viscous and heat conducting solutions. In other words, the highly non-equilibrium of the gas distribution function in the discontinuous region provides a physically consistent mechanism for the construction of a numerical shock structure. In this sense, the GKS is close to the methodology of artificial dissipation approach, but with different dissipative mechanism. In smooth flow region, the hydrodynamic scale physics corresponding to the multi-dimensional central difference discretization captures the accurate viscous solutions. Due to the coupling of inviscid and viscous terms in the kinetic formulation, theoretically there is no difficulty for GKS to capture NS solutions in any structure or unstructured mesh. With the discretization of particle velocity space, a unified gas-kinetic scheme (UGKS) has been developed for the flow study in entire flow regime from rarefied to continuum ones [25, 18, 9].

Recently, with the incorporation of high-order initial data reconstruction, a higher-order gas-kinetic schemes has been proposed in [16, 15, 17]. The flux evaluation in the scheme is based on the time evolution of flow variables from an initial piece-wise discontinuous polynomials (parabola) around a cell interface, where higher-order spatial and temporal derivatives of a gas distribution function are coupled nonlinearly. The whole curves of discontinuous flow distributions around a cell interface interact through particle transport and collision in the determination of the flux function. Besides the evaluation of the time-dependent flux function across a cell interface, the higher-order gas evolution model also provides an accurate time-dependent solution of flow variables at a cell interface as well. Thus, it is feasible to develop a compact scheme with the consideration of time evolution of both cell averaged and cell interface flow variables. A compact third-order gas-kinetic scheme is proposed for the compressible Euler and Navier-Stokes equations on structure meshes with WENO-type reconstruction [20]. However, this reconstruction technique is difficult to be used on unstructured meshes. Therefore, on the unstructured meshes, a weighted least-square reconstruction will be used in this paper. To the third-order accuracy, a quadratic distribution for the flow variables inside each cell needs to be determined. Based on the cell averaged and cell interface values of neighboring cells only, an over-determined linear system is formed. With the least-square solution for the system, the whole flow distribution can be fully determined. The shock detector can be also used as well to switch between higher-order (3rd) and lower order (2nd) reconstructions in different regions. In comparison with traditional schemes, the Gaussian points for the flux evaluation along the cell interface and the multi-stage Runge-Kutta technique are avoided in the current compact method. At

the same time, the current third-order compact scheme is stable under the CFL condition  $\text{CFL} \simeq 0.5$ .

This paper is organized as follows. In Section 2, the finite volume scheme on the unstructured mesh and third-order GKS are introduced. In section 3, the compact reconstruction on the triangular mesh is presented, and the techniques can be applied to rectangular mesh as well. Section 4 includes numerical examples to validate the current algorithm. The last section is the conclusion.

## 2. Finite volume gas-kinetic scheme

### 2.1. Finite volume scheme

The two-dimensional gas-kinetic BGK equation can be written as [3],

$$f_t + \mathbf{u} \cdot \nabla f = \frac{g - f}{\tau}, \quad (1)$$

where  $f$  is the gas distribution function,  $g$  is the corresponding equilibrium state, and  $\tau$  is the collision time. The collision term satisfies the compatibility condition

$$\int \frac{g - f}{\tau} \varphi d\Xi = 0, \quad (2)$$

where  $\varphi = (1, u, v, \frac{1}{2}(u^2 + v^2 + \xi^2))$ ,  $d\Xi = du dv d\xi^1 \dots d\xi^K$ ,  $K$  is the number of internal freedom, i.e.  $K = (4 - 2\gamma)/(\gamma - 1)$  for two-dimensional flows, and  $\gamma$  is the specific heat ratio.

Based on the Chapman-Enskog expansion of the BGK model, the Euler and Navier-Stokes, Burnett, and Super-Burnett equations can be derived [4, 23]. In the smooth region, the gas distribution function can be expanded as

$$f = g - \tau D_{\mathbf{u}} g + \tau D_{\mathbf{u}} (\tau D_{\mathbf{u}}) g - \tau D_{\mathbf{u}} [\tau D_{\mathbf{u}} (\tau D_{\mathbf{u}}) g] + \dots,$$

where  $D_{\mathbf{u}} = \partial/\partial t + \mathbf{u} \cdot \nabla$ . By truncating different orders of  $\tau$ , the corresponding macroscopic equations can be derived. For the Euler equations, the zeroth order truncation is taken, i.e.  $f = g$ . For the Navier-Stokes equations, the first order truncation is

$$f = g - \tau(ug_x + vg_y + g_t). \quad (3)$$

Based on the higher order truncations, the Burnett and super-Burnett equations can be obtained.

In the computation, the computational volumes are simply triangles. For a control volume  $\Omega_i$ , its boundary is given by three line segments

$$\partial\Omega_i = \bigcup_m \Gamma_{im}.$$

Thus, taking moments of the kinetic equation Eq.(1) and integrating with respect to time and space, the finite volume scheme can be expressed as

$$W_i^{n+1} = W_i^n - \frac{1}{|\Omega_i|} \int_{t^n}^{t^{n+1}} \sum_m F_{im}(t) dt, \quad (4)$$

where  $W = (\rho, \rho U, \rho V, \rho E)$  are the conservative variables,  $F_{im}(t) = (F_\rho, F_{\rho u}, F_{\rho v}, F_E)$  are the fluxes across the cell interface  $\Gamma_{im}$  in the global coordinate, which is defined as

$$F_{im}(t) = \int_{\Gamma_{im}} \left( \int \varphi f(x, y, t, u, v, \xi) \mathbf{u} \cdot \mathbf{n} du dv d\xi \right) ds. \quad (5)$$

where  $\mathbf{n} = (\cos \theta, \sin \theta)$  is the outer normal direction of the cell interface  $\Gamma_{im}$ , and the tangential direction is denoted as  $\mathbf{t} = (-\sin \theta, \cos \theta)$ . Eq.(4) is valid in any scale if the interface flux is properly defined, which is beyond the validity of the Navier-Stokes equations.

According to the coordinate transformation, the local coordinate for the cell interface  $\Gamma_{im}$  is expressed as  $(\tilde{x}, \tilde{y}) = (0, \tilde{y})$ , where  $\tilde{y} \in [-d, d]$  and  $d = |\Gamma_{im}|/2$ , and the velocities in the local coordinate are given by

$$\begin{cases} \tilde{u} = u \cos \theta + v \sin \theta, \\ \tilde{v} = -u \sin \theta + v \cos \theta. \end{cases} \quad (6)$$

For the gas distribution function in the local coordinate,  $\tilde{f}(\tilde{x}, \tilde{y}, t, \tilde{u}, \tilde{v}, \xi) = f(x, y, t, u, v, \xi)$  and  $du dv = d\tilde{u} d\tilde{v}$ , then the line integral for the gas distribution function over the cell interface  $\Gamma_{im}$  can be transformed as

$$\int_{\Gamma_{im}} \int \varphi f(x, y, t, u, v, \xi) \mathbf{u} \cdot \mathbf{n} du dv d\xi ds = \int_{-d}^d \int \varphi \tilde{f}(0, \tilde{y}, t, \tilde{u}, \tilde{v}, \xi) \tilde{u} d\tilde{u} d\tilde{v} d\xi d\tilde{y}. \quad (7)$$

Thus, in the computation, the numerical fluxes in the local coordinate  $\tilde{F}(t) = (F_{\tilde{\rho}}, F_{\tilde{m}}, F_{\tilde{n}}, F_{\tilde{E}})$  are obtained first by taking moments of the gas distribution function in the local coordinate

$$\tilde{F}(t) = \int_{-d}^d \int \tilde{u} \tilde{\varphi} \tilde{f}(0, \tilde{y}, t, \tilde{u}, \tilde{v}, \xi) d\tilde{u} d\tilde{v} d\xi d\tilde{y}, \quad (8)$$

where  $\tilde{\varphi} = (1, \tilde{u}, \tilde{v}, \frac{1}{2}(\tilde{u}^2 + \tilde{v}^2 + \xi^2))$ . According to Eq.(6) and Eq.(7), the fluxes in the global coordinate can be expressed as a combination of the fluxes in the local coordinate

$$\begin{cases} F_\rho = F_{\tilde{\rho}}, \\ F_m = F_{\tilde{m}} \cos \theta - F_{\tilde{n}} \sin \theta, \\ F_n = F_{\tilde{m}} \sin \theta + F_{\tilde{n}} \cos \theta, \\ F_E = F_{\tilde{E}}. \end{cases} \quad (9)$$

With the above numerical fluxes at the cell interface, the flow variables inside each control volume can be updated according to Eq.(4).

## 2.2. Gas-kinetic flux solver

In this section, the numerical flux will be presented in the local coordinate. For simplicity, all notations with tilde will be omitted here after.

In order to simulate the NS solutions, we need to model the interface flux function. For the distribution function at a cell interface, the integral solution of BGK equation Eq.(1) at the cell interface in the local coordinate can be written as

$$f(0, y, t, u, v, \xi) = \frac{1}{\tau} \int_0^t g(x', y', t', u, v, \xi) e^{-(t-t')/\tau} dt' + e^{-t/\tau} f_0(-ut, y - vt, u, v, \xi), \quad (10)$$

where  $x = 0$  is the location of the cell interface,  $x = x' + u(t - t')$  and  $y = y' + v(t - t')$  are the trajectory of particles,  $f_0$  is the initial gas distribution function, and  $g$  is the corresponding equilibrium state. The target equations to be solved depend on the modeling of the initial condition  $f_0$  term.

To construct a multidimensional third-order gas-kinetic solver, the following notations are introduced firstly

$$\begin{aligned} a_1 &= (\partial g / \partial x) / g, a_2 = (\partial g / \partial y) / g, A = (\partial g / \partial t) / g, B = (\partial A / \partial t), \\ d_{11} &= (\partial a_1 / \partial x), d_{12} = (\partial a_1 / \partial y) = (\partial a_2 / \partial x), d_{22} = (\partial a_2 / \partial y), \\ b_1 &= (\partial a_1 / \partial t) = (\partial A / \partial x), b_2 = (\partial a_2 / \partial t) = (\partial A / \partial y), \end{aligned}$$

where  $g$  is an equilibrium state. The dependence of these coefficients on particle velocity can be expanded as the following form [24]

$$\begin{aligned} a_1 &= a_{11} + a_{12}u + a_{13}v + a_{14}\frac{1}{2}(u^2 + v^2 + \xi^2), \\ &\dots \\ B &= B_1 + B_2u + B_3v + B_4\frac{1}{2}(u^2 + v^2 + \xi^2). \end{aligned}$$

For the kinetic part of the integral solution Eq.(10), the gas distribution function can be constructed as

$$f_0 = f_0^l(x, y, u, v)H(x) + f_0^r(x, y, u, v)(1 - H(x)), \quad (11)$$

where  $H(x)$  is the Heaviside function,  $f_0^l$  and  $f_0^r$  are the initial gas distribution functions on both sides of a cell interface, which have one to one correspondence with the initially reconstructed polynomials of macroscopic flow variables on both sides of the cell interface. To construct a third-order scheme, the Taylor expansion for the gas distribution function in

space and time at  $(x, y) = (0, 0)$  is expressed as

$$f_0^k(x, y) = f_G^k(0, 0) + \frac{\partial f_G^k}{\partial x}x + \frac{\partial f_G^k}{\partial y}y + \frac{1}{2}\frac{\partial^2 f_G^k}{\partial x^2}x^2 + \frac{\partial^2 f_G^k}{\partial x \partial y}xy + \frac{1}{2}\frac{\partial^2 f_G^k}{\partial y^2}y^2,$$

where  $k = l, r$ . For the Euler equations,  $f_G^k = g_k$  and the kinetic part of Eq.(10) can be obtained. For the Navier-Stokes equations, according to Eq.(3) and the notations introduced above, the distribution function is

$$f_G^k = g_k - \tau(a_{1k}u + a_{2k}v + A_k)g_k,$$

where  $g_l, g_r$  are the equilibrium states corresponding to the macroscopic variables  $W_l, W_r$  given by the reconstruction procedure at both sides of cell interface. Thus, the corresponding kinetic part of Eq.(10) can be written as

$$\begin{aligned} & e^{-t/\tau} f_0^k(-ut, y - vt, u, v) \\ &= C_7 g_k [1 - \tau(a_{1k}u + a_{2k}v + A_k)] \\ &+ C_8 g_k [a_{1k}u - \tau((a_{1k}^2 + d_{11k})u^2 + (a_{1k}a_{2k} + d_{12k})uv + (A_k a_{1k} + b_{1k})u)] \\ &+ C_8 g_k [a_{2k}v - \tau((a_{1k}a_{2k} + d_{12k})uv + (a_{2k}^2 + d_{22k})v^2 + (A_k a_{2k} + b_{2k})v)] \\ &+ C_7 g_k [a_{2k} - \tau((a_{1k}a_{2k} + d_{12k})u + (a_{2k}^2 + d_{22k})v + (A_k a_{2k} + b_{2k}))]y \\ &+ \frac{1}{2} C_7 g_k [(a_{1k}^2 + d_{11k})(-ut)^2 + 2(a_{1k}a_{2k} + d_{12k})(-ut)(y - vt) + (a_{2k}^2 + d_{22k})(y - vt)^2], \quad (12) \end{aligned}$$

where  $g_k$  are the equilibrium states at both sides of the cell interface, and the coefficients  $a_{1k}, \dots, A_k$  are defined according to the expansion of  $g_k$ .

After determining the kinetic part  $f_0$ , the equilibrium state  $g$  in the integral solution Eq.(10) can be constructed as follows

$$\begin{aligned} g = g_0 &+ \frac{\partial g_0}{\partial x}x + \frac{\partial g_0}{\partial y}y + \frac{\partial g_0}{\partial t}t + \frac{1}{2}\frac{\partial^2 g_0}{\partial x^2}x^2 + \frac{\partial^2 g_0}{\partial x \partial y}xy + \frac{1}{2}\frac{\partial^2 g_0}{\partial y^2}y^2 \\ &+ \frac{1}{2}\frac{\partial^2 g_0}{\partial t^2}t^2 + \frac{\partial^2 g_0}{\partial x \partial t}xt + \frac{\partial^2 g_0}{\partial y \partial t}yt, \quad (13) \end{aligned}$$

where  $g_0$  is the equilibrium state located at interface, which can be determined through the compatibility condition Eq.(2)

$$\int \psi g_0 d\Xi = W_0 = \int_{u>0} \psi g_l d\Xi + \int_{u<0} \psi g_r d\Xi. \quad (14)$$

Based on Taylor expansion for the equilibrium state Eq.(13), the hydrodynamic part in

Eq.(10) can be written as

$$\begin{aligned}
& \frac{1}{\tau} \int_0^t g(x', y', t', u, v) e^{-(t-t')/\tau} dt' \\
& = C_1 g_0 + C_2 g_0 \bar{a}_1 u + C_2 g_0 \bar{a}_2 v + C_1 g_0 \bar{a}_2 y + C_3 g_0 \bar{A} \\
& + \frac{1}{2} C_4 g_0 (\bar{a}_1^2 + \bar{d}_{11}) u^2 + C_6 g_0 (\bar{A} \bar{a}_1 + \bar{b}_1) u + \frac{1}{2} C_5 g_0 (\bar{A}^2 + \bar{B}) \\
& + \frac{1}{2} C_1 g_0 (\bar{a}_2^2 + \bar{d}_{22}) y^2 + C_2 g_0 (\bar{a}_2^2 + \bar{d}_{22}) v y + \frac{1}{2} C_4 g_0 (\bar{a}_2^2 + \bar{d}_{22}) v^2 \\
& + C_2 g_0 (\bar{a}_1 \bar{a}_2 + \bar{d}_{12}) u y + C_4 g_0 (\bar{a}_1 \bar{a}_2 + \bar{d}_{12}) u v \\
& + C_3 g_0 (\bar{A} \bar{a}_2 + \bar{b}_2) y + C_6 g_0 (\bar{A} \bar{a}_2 + \bar{b}_2) v,
\end{aligned} \tag{15}$$

where the coefficients  $\bar{a}_1, \bar{a}_2, \dots, \bar{A}, \bar{B}$  are defined from the expansion of the equilibrium state  $g_0$ . The coefficients  $C_i, i = 1, \dots, 8$  in Eq.(15) and Eq.(12) are given by

$$\begin{aligned}
C_1 &= 1 - e^{-t/\tau}, C_2 = (t + \tau) e^{-t/\tau} - \tau, C_3 = t - \tau + \tau e^{-t/\tau}, C_4 = -(t^2 + 2t\tau) e^{-t/\tau}, \\
C_5 &= t^2 - 2t\tau, C_6 = -t\tau(1 + e^{-t/\tau}), C_7 = e^{-t/\tau}, C_8 = -t e^{-t/\tau}.
\end{aligned}$$

Substituting Eq.(15) and Eq.(12) into the integral solution Eq.(10), the gas distribution function at the cell interface can be obtained. The superscripts or subscripts of the coefficients  $a_1, a_2, \dots, A, B$  in Eq.(12) and Eq.(15) are omitted for simplicity and they are determined by the spatial derivatives of macroscopic flow variables and the compatibility condition [15] as follows

$$\begin{cases}
\langle a_1 \rangle = \frac{\partial W}{\partial x}, \langle a_2 \rangle = \frac{\partial W}{\partial y}, \langle A + a_1 u + a_2 v \rangle = 0, \\
\langle a_1^2 + d_{11} \rangle = \frac{\partial^2 W}{\partial x^2}, \langle a_2^2 + d_{22} \rangle = \frac{\partial^2 W}{\partial y^2}, \langle a_1 a_2 + d_{12} \rangle = \frac{\partial^2 W}{\partial x \partial y}, \\
\langle (a_1^2 + d_{11})u + (a_1 a_2 + d_{12})v + (A a_1 + b_1) \rangle = 0, \\
\langle (a_1 a_2 + d_{12})u + (a_2^2 + d_{22})v + (A a_2 + b_2) \rangle = 0, \\
\langle (A a_1 + b_1)u + (A a_2 + b_2)v + (A^2 + B) \rangle = 0,
\end{cases} \tag{16}$$

where  $\langle \dots \rangle$  are the moments of gas distribution function, and defined by

$$\langle \dots \rangle = \int g(\dots) \psi d\Xi.$$

In the following section, with the reconstruction procedure, the conservative value  $W_l, W_r$  and  $W_0$  at the center of cell interface corresponding to the equilibrium  $g_l, g_r, g_0$  and the derivatives in Eq.(16) will be presented.

### 3. Compact reconstruction

This paper focuses on the high-order compact finite volume scheme. In the finite volume type schemes, to achieve higher-order accuracy, a reconstruction for the flow variables with high-order polynomials inside each cell is needed as the initial condition at the beginning of each time step. For the higher-order reconstruction, a large number of stencils is usually needed to determine all degrees of freedom through the WENO or least square techniques [1, 7, 6, 2, 19]. In this section, the reconstruction will be done for the unstructured mesh with a compact stencil, which is shown in Fig.1. For simplicity, the whole reconstruction procedure is performed in a local coordinate  $(x, y)$  relative to a cell interface, such as AB in Fig.1, which is consistent with the evaluation of a time-dependent gas distribution function at the cell interface.

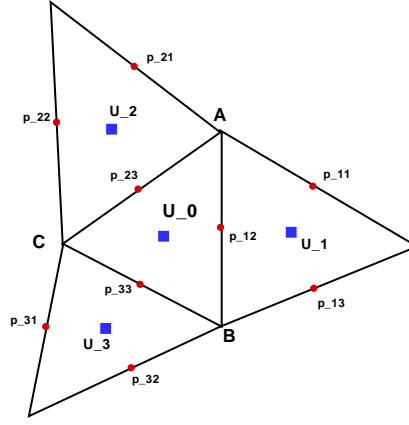


Figure 1: The stencil of a compact reconstruction for triangle  $\Omega_0 = \triangle ABC$ . The blue squares are the cell averaged values and the red circles are point values at the center of cell interface.

In the gas-kinetic scheme, besides the numerical fluxes, the macroscopic pointwise values at a cell interface in the local coordinate can be obtained by taking moments of the gas distribution function,

$$W(t, y) = \int \varphi f(x_{i+1/2}, y, t, u, v, \xi) du dv d\xi. \quad (17)$$

As shown in the last section, the whole curve of the polynomial of the macroscopic variables will participate the flow evolution, and the spatial and temporal derivatives of the gas distribution function are coupled nonlinearly. This point-wise value at the cell interface Eq.(17) is a solution of the evolution model, which can be used in the reconstruction stage at the beginning of next time step. Thus, in the following subsections, a third-order compact reconstruction will be presented for the unstructured mesh, in which the pointwise values at the cell interface and the cell averaged values shown in Fig.1 are used in the reconstruction.



The macroscopic variables for reconstruction is denoted by  $U$ . For the smooth flow, the conservative variables  $W$  will be directly used for reconstruction, i.e.  $U = W$ . For the flow with discontinuity, in order to eliminate the spurious oscillation and improve the stability of the scheme, the compact reconstruction is based on the characteristic variables. Denote  $F(W) = (\rho U, \rho U^2 + p, \rho UV, U(\rho E + p))$  in the local coordinate. The Jacobian matrix  $\partial F / \partial W$  can be diagonalized by the right eigenmatrix  $R$ , and the characteristic variables is defined as  $U = R^{-1}W$ . For a cell interface,  $R$  is the right eigenmatrix for  $\partial F / \partial W^*$  and  $W^*$  is the averaged conservative value from both side of cell interface. To the third order accuracy, the expansion of the macroscopic variable  $U$  inside the cell  $\Omega_0$  can be expressed as

$$\begin{aligned} U(x, y) = & U_0 + U_x((x - x_0) - \widehat{x}_0) + U_y((y - y_0) - \widehat{y}_0) + \frac{1}{2}U_{xx}((x - x_0)^2 - \widehat{x}_0^2) \\ & + U_{xy}((x - x_0)(y - y_0) - \widehat{x}_0\widehat{y}_0) + \frac{1}{2}U_{yy}((y - y_0)^2 - \widehat{y}_0^2), \end{aligned} \quad (18)$$

where  $(x_0, y_0)$  is the barycenter of  $\Omega_0$ ,  $U_0$  is the cell averaged value for  $U(x, y)$ , and

$$\widehat{x^m y^n} = \frac{1}{|\Omega_0|} \int_{\Omega_0} (x - x_0)^n (y - y_0)^m dV.$$

The cell averaged value for the base function over the triangle  $\Omega_i$  is denoted as

$$\widehat{x^m y^n}_i = \frac{1}{|\Omega_i|} \int_{\Omega_i} ((x - x_0)^n (y - y_0)^m - \widehat{x^m y^n}) dV. \quad (19)$$

and the point-wise value for the base function at the point  $p_{ij} = (x_{ij}, y_{ij})$  is denoted as

$$x^m y^n_{ij} = ((x_{ij} - x_0)^n (y_{ij} - y_0)^m - \widehat{x^m y^n}). \quad (20)$$

### 3.1. Initial data reconstruction

In this subsection, the weighted least-square reconstruction will be presented for the initial data reconstruction. As shown in Fig.1, three cell averaged values  $U_i, i = 1, 2, 3$  (blue square) form the neighboring cells and nine point-wise values  $U_{ij}, i, j = 1, 2, 3$  (red circle) from the cell interface will be used in the weighted least square reconstruction.

For the third order expansion, with the definition of the cell averaged and point-wise values for the base function Eq.(19) and Eq.(20), we have

$$U_x \widehat{x}_i + U_y \widehat{y}_i + \frac{1}{2}U_{xx} \widehat{x}_i^2 + U_{xy} \widehat{x}_i \widehat{y}_i + \frac{1}{2}U_{yy} \widehat{y}_i^2 = U_i - U_0, \quad (21)$$

where  $U_i$  is the cell averaged value for the neighboring triangle  $\Omega_i, i = 1, 2, 3$ . For the nine cell interface points  $p_{ij}, i, j = 1, 2, 3$ , we have

$$U_x x_{ij} + U_y y_{ij} + \frac{1}{2}U_{xx} x_{ij}^2 + U_{xy} x_{ij} y_{ij} + \frac{1}{2}U_{yy} y_{ij}^2 = U_{ij} - U_0, \quad (22)$$

where  $U_{ij}$  is the point-wise value of  $U(x, y)$  at the point  $p_{ij}$ .

To solve the corresponding derivatives for  $U(x, y)$ , Eq.(21) and Eq.(22) can be written into an over-determined linear system

$$\begin{pmatrix} \hat{x}_1 & \hat{y}_1 & \frac{1}{2}\hat{x}_1^2 & \hat{x}\hat{y}_1 & \frac{1}{2}\hat{y}_1^2 \\ \cdots & \cdots & \cdots & \cdots & \cdots \\ \hat{x}_3 & \hat{y}_3 & \frac{1}{2}\hat{x}_3^2 & \hat{x}\hat{y}_3 & \frac{1}{2}\hat{y}_3^2 \\ x_{11} & y_{11} & \frac{1}{2}x_{11}^2 & xy_{11} & \frac{1}{2}y_{11}^2 \\ \cdots & \cdots & \cdots & \cdots & \cdots \\ x_{33} & y_{33} & \frac{1}{2}x_{33}^2 & xy_{33} & \frac{1}{2}y_{33}^2 \end{pmatrix} \cdot \begin{pmatrix} U_x \\ U_y \\ U_{xx} \\ U_{xy} \\ U_{yy} \end{pmatrix} = \begin{pmatrix} U_1 - U_0 \\ \cdots \\ U_3 - U_0 \\ U_{11} - U_0 \\ \cdots \\ U_{33} - U_0 \end{pmatrix}. \quad (23)$$

Denote  $dU = (U_x, U_y, U_{xx}, U_{xy}, U_{yy})^T$ ,  $\Delta U = (U_1 - U_0, \dots, U_3 - U_0, U_{11} - U_0, \dots, U_{33} - U_0)^T$ , the above linear system is expressed as the matrix form

$$DdU = \Delta U.$$

where  $D$  is the coefficient matrix corresponding to Eq.(23).

To deal with the discontinuity, a diagonal matrix  $W$  is introduced as the simple weight functions

$$w_i = \frac{1}{(s_i^2 + \epsilon)}, \quad w_{ij} = \frac{1}{(s_{ij}^2 + \epsilon)}$$

where  $s_i = \frac{U_i - U_0}{|\mathbf{x}_i - \mathbf{x}_0|}$ ,  $s_{ij} = \frac{U_{ij} - U_0}{|\mathbf{x}_i - \mathbf{x}_0|}$ ,  $i, j = 1, \dots, 3$ , and  $\epsilon = 10^{-6}$ . The derivatives  $dU$  can be obtained by solving the linear system

$$D^T W D dU = D^T W \Delta U.$$

Generally, for most cases with Mach number  $Ma < 2$ , the weight function is enough to deal with the discontinuity. However, for strong discontinuity, the shock detection [13] technique is used in the current scheme. Analogous to the analysis of KXRCF detector [13], for the third-order scheme, it is easy to distinguish the smooth region from the region near discontinuities as follows

$$U_i(x_i) - U_{j \rightarrow i}(x_i) = \begin{cases} O(h^3) & \text{in smooth region,} \\ O(h) & \text{near discontinuity,} \end{cases}$$

where the index  $i$  refers  $\Delta_{ABC}$  and the index  $j$  refers  $\Delta_{ABC'}$ ,  $U_i(x_i)$  is the interpolated value at the center of  $\Delta_{ABC}$  and  $U_{j \rightarrow i}(x_i)$  is the value at the center of  $\Delta_{ABC}$  extrapolated from  $\Delta_{ABC'}$ . In the computation, the "trouble cell" is detected according the following criterion

$$\max(\|U_i(x_i) - U_{j \rightarrow i}(x_i)\|, \|U_j(x_j) - U_{i \rightarrow j}(x_j)\|) \geq C \sqrt{S_{\Delta_{ABC}} + S_{\Delta_{ABC'}}} \sim O(h),$$

where  $S$  is the area of the triangle,  $C$  is a problem dependent coefficient, and  $C = 5$  is used in the computation. In those detected "trouble cell", the second order scheme with limiters are used. The above choice of weight functions may not be optimal and further study is needed.

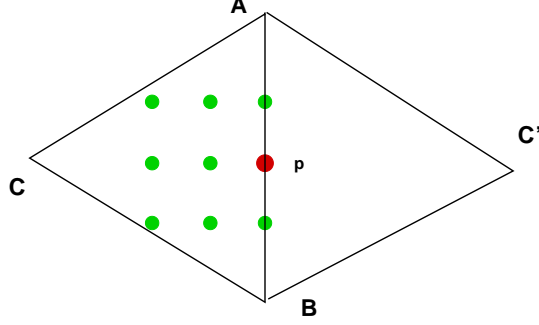


Figure 2: The stencil of the compact reconstruction for triangle  $\Omega_0 = \Delta_{ABC}$  for the characteristic variables. The coordinate of these points  $p_{ij}$ ,  $i, j = 1, 2, 3$  is  $((i - 3)d, (j - 2)d)$ , where  $d = d_{AB}/4$ .

With the derivatives  $dU = (U_x, U_y, U_{xx}, U_{xy}, U_{yy})^T$ , the whole flow distribution in the cell  $\Delta_{ABC}$  in Fig.2 can be obtained. For the smooth flow, no special treatment is needed. With  $W = U$ , the interpolated value  $W_l$  and the derivatives  $dW_l$  can be fully obtained in the cell  $\Delta_{ABC}$ . Similarly, the interpolated value  $W_r$  and the derivatives  $dW_r$  in the cell  $\Delta_{ABC'}$  can be obtained as well.

For the flow with discontinuity, the characteristic variables are reconstructed in the cell  $\Delta_{ABC}$ . With the derivatives  $dU = (U_x, U_y, U_{xx}, U_{xy}, U_{yy})^T$ , the interpolated value  $U$  at the points in Fig.2 can be obtained. By the inverse projection, the conservative variables  $W = RU$ , where  $R$  is the right eigenmatrix. Based on these point-wise values and their central difference,  $W_l$  and  $dW_l$  can be obtained. Similarly, the interpolated value  $W_r$  and the derivatives  $dW_r$  in the cell  $\Delta_{ABC'}$  can be also obtained.

### 3.2. Reconstruction for equilibrium part

In this subsection, the reconstruction for the equilibrium part will be presented. This reconstruction will be based on the conservative variables  $W$ . To the third-order accuracy, the Taylor expansion corresponding to equilibrium part at the center point of a cell interface is expressed as

$$\begin{aligned} \overline{W}(x, y) = & W_0 + \overline{W}_x(x - x_p) + \overline{W}_y(y - y_p) \\ & + \frac{1}{2}\overline{W}_{xx}(x - x_p)^2 + \overline{W}_{xy}(x - x_p)(y - y_p) + \frac{1}{2}\overline{W}_{yy}(y - y_p)^2, \end{aligned} \quad (24)$$

where  $W_0$  is the conservative variable at the center point of cell interface  $AB$  based on the compatibility condition Eq.(14), and  $\overline{W}_x, \dots, \overline{W}_{yy}$  are corresponding derivatives.

As shown in Fig.3, with the reconstructed polynomials in  $\Delta_{ABC}$  and  $\Delta_{ABC'}$ , the point values at those points can be determined, which has been obtained in the last subsection.

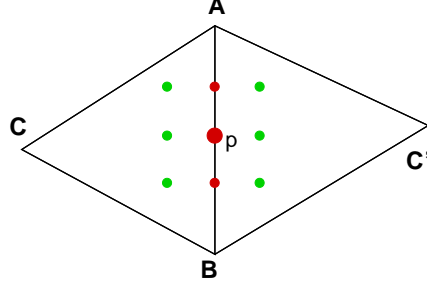


Figure 3: The stencil for the equilibrium part in the local coordinate. The coordinate of these points  $p_{ij}, i, j = 1, 2, 3$  is  $((i-2)d, (j-2)d)$ , where  $d = d_{AB}/4$ .

Especially, we can get the point values at the interface (red) points at both sides of  $AB$ . By the compatibility condition Eq.(2), the reconstructed conservative variables at the cell interface can be determined. The derivatives  $\overline{W}_x, \dots, \overline{W}_{yy}$  can be obtained by the central difference of these point-wise values.

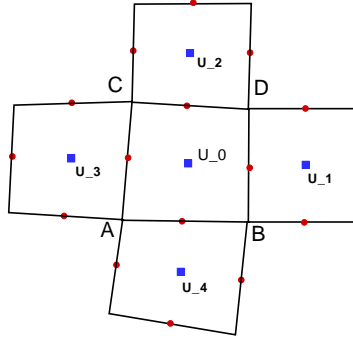


Figure 4: The stencil for the rectangular mesh. The red circles represent the point-wise value and the blue squares are the cell averaged values.

### 3.2.1. Extension to rectangular mesh

For the rectangular mesh, the stencils are given in Fig.4. To reconstruct the polynomial for the rectangular  $\square_{ABCD}$ , the cell averaged values  $U_i, i = 1, 2, 3, 4$  and point-wise values  $p_{ij}, i, j = 1, 2, 3, 4$  at the cell interfaces can be used. Similar to the triangular case, we have the following matrix form for the over-determined linear system

$$D_2 dU = \Delta U.$$

where  $dU = (U_x, U_y, U_{xx}, U_{xy}, U_{yy})^T$ ,  $\Delta U = (U_1 - U_0, \dots, U_4 - U_0, U_{11} - U_0, \dots, U_{44} - U_0)^T$ .  $D_2$  is the coefficient matrix and expressed as

$$D_2 = \begin{pmatrix} \widehat{x}_1 & \widehat{y}_1 & \frac{1}{2}\widehat{x}_1^2 & \widehat{x}\widehat{y}_1 & \frac{1}{2}\widehat{y}_1^2 \\ & & \dots & & \\ \widehat{x}_4 & \widehat{y}_4 & \frac{1}{2}\widehat{x}_4^2 & \widehat{x}\widehat{y}_4 & \frac{1}{2}\widehat{y}_4^2 \\ x_{11} & y_{11} & \frac{1}{2}x_{11}^2 & xy_{11} & \frac{1}{2}y_{11}^2 \\ & & \dots & & \\ x_{14} & y_{44} & \frac{1}{2}x_{44}^2 & xy_{44} & \frac{1}{2}y_{44}^2 \end{pmatrix}$$

By introducing the weight diagonal matrix  $W$ , the derivative  $dU$  can be also obtained by solving the following linear system

$$D_2^T W D_2 dU = D_2^T W \Delta U.$$

The limiting process is also used for the flow with large discontinuity. In some cases of the numerical tests, the solutions from the compact scheme with rectangular mesh will be presented as well.

#### 4. Numerical tests

In this section, numerical tests for both inviscid flow and viscous flow will be presented to validate the compact scheme. For the inviscid flow, the collision time  $\tau$  takes

$$\tau = \epsilon \Delta t + C \left| \frac{p_l - p_r}{p_l + p_r} \right| \Delta t,$$

where  $\epsilon = 0.05$  and  $C = 1$ . For the viscous flow, we have

$$\tau = \frac{\mu}{p} + C \left| \frac{p_l - p_r}{p_l + p_r} \right| \Delta t,$$

where  $p_l$  and  $p_r$  denotes the pressure on the left and right sides of the cell interface,  $\mu$  is the viscous coefficient,  $p$  is the pressure at the cell interface and  $C = 1$ . In the smooth flow regions, it will reduce to  $\tau = \mu/p$ . The ratio of specific heats takes  $\gamma = 1.4$ .  $\Delta t$  is the time step which is determined according to the CFL condition. In the numerical tests, the CFL number takes a value of 0.35, even though the scheme works as well with a large CFL number. The value of 0.35 is already more than two times of the time step used for the compact third-order DG method.

##### 4.1. Accuracy test

The numerical order of the compact gas-kinetic scheme is tested in comparison with the analytical solutions of the Euler equations. The isotropic vortex propagation problem is presented to validate the accuracy for the solution of inviscid flow. The computational domain is taken to be  $[0, 1.5] \times [0, 1.5]$ . The free upstream is  $(\rho, u, v, p) = (1.21, 0, 0, 1)$ , and

a small vortex is obtained through a perturbation on the mean flow with the velocity  $(u, v)$ , temperature  $T = p/\rho$ , and entropy  $S = \ln(p/\rho^\gamma)$ . The perturbation is expressed as

$$\begin{aligned}(\delta u, \delta v) &= \kappa \eta e^{\mu(1-\eta^2)} (\sin \theta, -\cos \theta), \\ \delta T &= -\frac{(\gamma-1)\kappa^2}{4\mu\gamma} e^{2\mu(1-\eta^2)}, \delta S = 0,\end{aligned}$$

where  $\eta = r/r_c$ ,  $r = \sqrt{(x-x_c)^2 + (y-y_c)^2}$ ,  $(x_c, y_c) = (0.75, 0.75)$ ,  $\kappa = 0.3$ ,  $\mu = 0.204$ , and  $r_c = 0.05$ . In the computation, the unstructured meshes with mesh size  $h = 1/30, 1/50, 1/100$  and  $1/200$  are used, and the  $L^\infty$  errors and orders at  $t = 1$  are presented in Table.1, which shows a third-order accuracy of the current compact scheme.

mesh	$L^\infty$ norm	order
1/30	3.2460690E-03	
1/50	7.3230267E-04	2.914901
1/100	9.2029572E-05	2.992271
1/200	1.1801720E-05	2.963100

Table 1: Accuracy test for the isotropic vortex problem.

#### 4.2. One dimensional Riemann problem

In this case, two one-dimensional Riemann problems are tested to verify the capability in capturing the wave configurations. The mesh is presented in Fig.5, where the computational domain is  $[0, 1] \times [0, 0.5]$ , and mesh size is around  $h = 0.01$ . The first one is Sod problem, and the initial condition is given by

$$(\rho, u, p) = \begin{cases} (1, 0, 1), & 0 < x < 0.5, \\ (0.125, 0, 0.1), & 0.5 < x < 1. \end{cases}$$

The second one is the Lax problem, and the initial condition is given as follows

$$(\rho, u, p) = \begin{cases} (0.445, 0.698, 3.528), & 0 \leq x < 0.5, \\ (0.5, 0, 0.571), & 0.5 \leq x \leq 1. \end{cases}$$

To compare with the exact solution, 100 points were extracted at  $y = 0.25$  for the Sod problem at  $t = 0.2$  and, for the Lax problem at  $t = 0.14$ . The density, velocity, and pressure distributions for the exact solutions and numerical results are presented in Fig.7, where the numerical results agree well with the exact solutions. The three dimensional density distributions for the two cases are given in Fig.6. In this case, the weighted least square reconstruction can deal with the discontinuity well, and the shock detection technique is not needed.

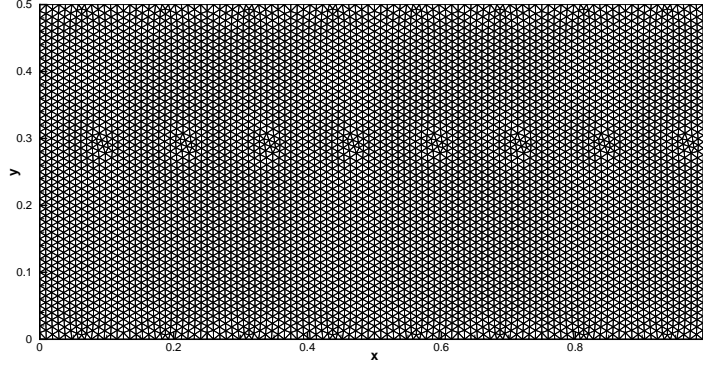


Figure 5: 1D Riemann problem: the mesh for the 1D Riemann problem.

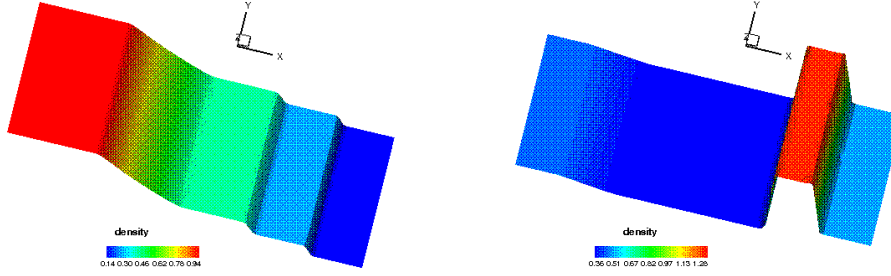


Figure 6: 1D Riemann problem: the 3d density distribution for the Sod problem (left) and Lax problem (right) in the computational domain.

#### 4.3. Flow impinging on a blunt body

In this case, the inviscid hypersonic flows impinging on a unit cylinder are tested to validate robustness of the current scheme. This problem is initialized by the flow moving towards a cylinder with different Mach numbers. The Euler boundary condition is imposed on the surface of cylinder, and outflow boundary condition on the right boundary. As mentioned in the reconstruction part, the weighted least square reconstruction is able to deal with the discontinuities at a Mach number  $Ma < 2$ . In this case, the flow with  $Ma = 1.9$  is tested without the detection of "trouble cell". The mesh and the pressure distribution for this case are also given in Fig.8, with mesh size  $h = 1/15$ , where the flow structure can be captured nicely in front of the cylinder. However, with a high Mach number, the weighted least square reconstruction is no longer able to capture strong discontinuities, and the shock detection technique is used to identify the trouble cells, where a second-order reconstruction is used in these cells. For the flow with  $Ma = 8$ , the mesh and the pressure distribution are shown in Fig.9 with mesh size  $h = 1/15$ . This test shows that the current scheme can capture the flow structure nicely in front of the cylinder and the carbuncle phenomenon does not appear [21].

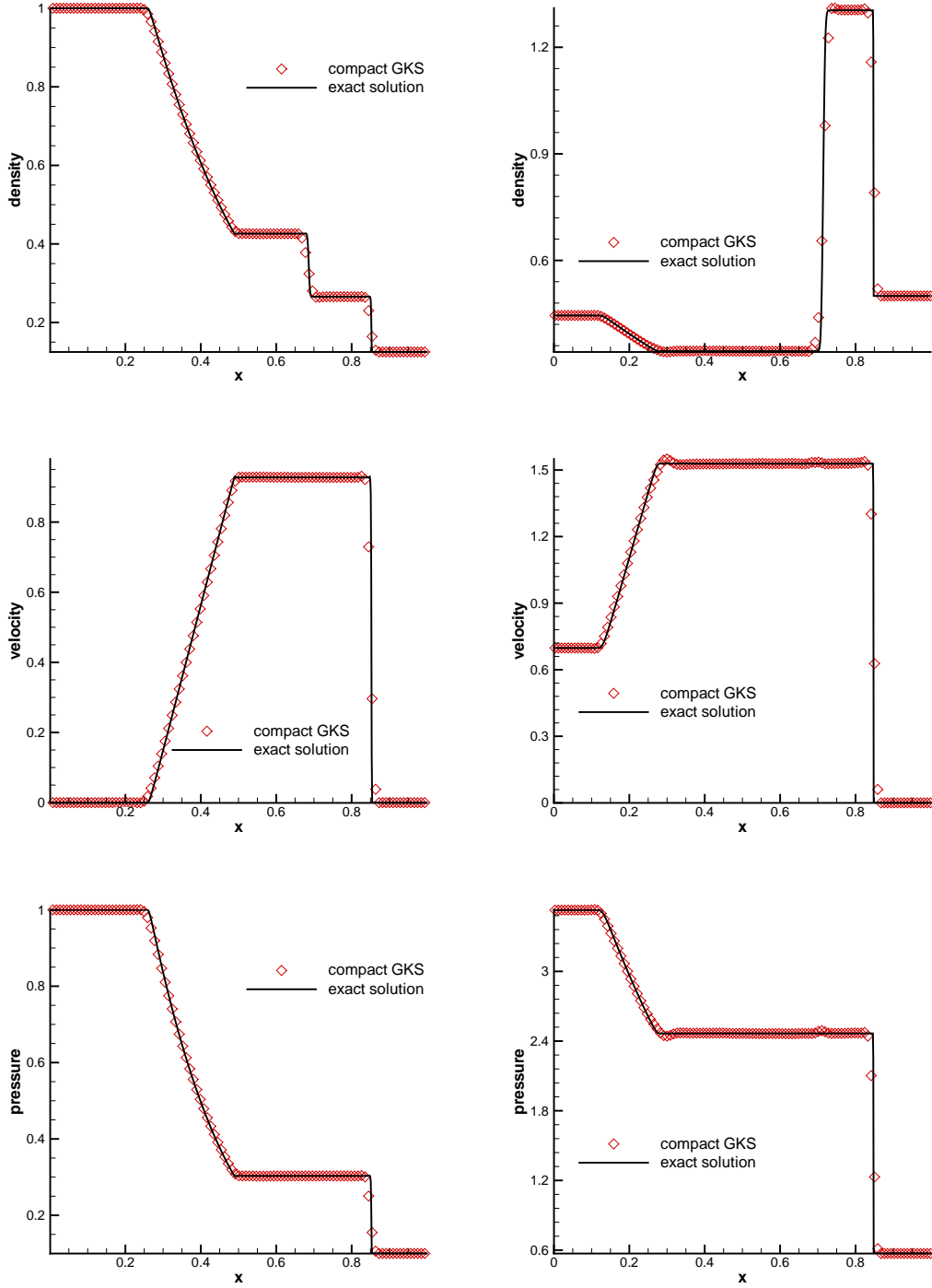


Figure 7: 1D Riemann problem: Sod problem (left): the density, velocity, and pressure distributions at  $t=0.2$ , and Lax problem (right): the density, velocity, and pressure distributions at  $t = 0.14$ , where the mesh size is  $h = 1/100$ .



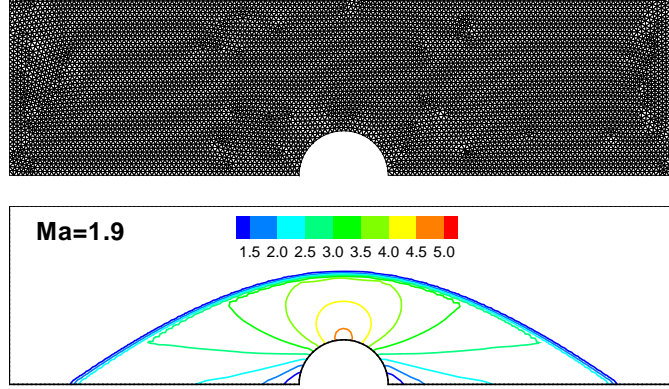


Figure 8: Flow impinging on a blunt body: the mesh and pressure distribution at  $Ma = 1.9$ .

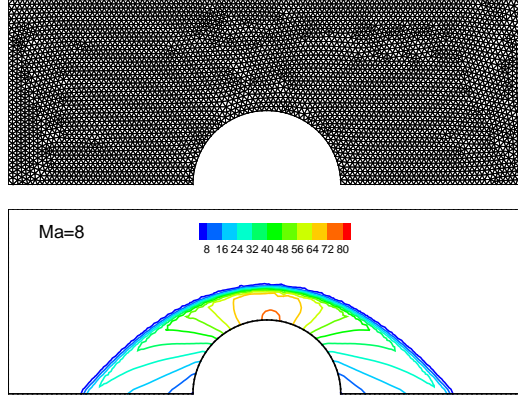


Figure 9: Flow impinging on a blunt body: the mesh and pressure distribution at  $Ma = 8$ .

#### 4.4. Shock vortex interaction

The interaction between a stationary shock and a vortex for the inviscid flow is presented [11]. The computational domain is taken to be  $[0, 1.5] \times [0, 1]$ . A stationary Mach 1.1 shock is positioned at  $x = 0.5$  and normal to the  $x$ -axis. The left upstream state is  $(\rho, u, v, p) = (Ma^2, \sqrt{\gamma}, 0, 1)$ , where  $Ma$  is the Mach number. A small vortex is obtained through a perturbation on the mean flow with the velocity  $(u, v)$ , temperature  $T = p/\rho$  and entropy  $S = \ln(p/\rho^\gamma)$ , and the perturbation is expressed as

$$\begin{aligned} (\delta u, \delta v) &= \kappa \eta e^{\mu(1-\eta^2)} (\sin \theta, -\cos \theta), \\ \delta T &= -\frac{(\gamma - 1)\kappa^2}{4\mu\gamma} e^{2\mu(1-\eta^2)}, \delta S = 0, \end{aligned}$$

where  $\eta = r/r_c$ ,  $r = \sqrt{(x - x_c)^2 + (y - y_c)^2}$ ,  $(x_c, y_c) = (0.25, 0.5)$  is the center of the vortex. Here  $\kappa$  indicates the strength of the vortex,  $\mu$  controls the decay rate of the vortex, and  $r_c$  is the critical radius for which the vortex has the maximum strength. In the computation,  $\kappa = 0.3$ ,  $\mu = 0.204$ , and  $r_c = 0.05$ . The reflected boundary conditions are used on the top and

bottom boundaries. The pressure distributions with mesh size  $h = 1/150$  at  $t = 0, 0.3, 0.6$  and  $0.8$  are shown in Fig.10. The detailed pressure distribution along the center horizontal line with mesh size  $h = 1/50, 1/100$ , and  $1/150$  at  $t = 0.8$  are shown in Fig.11. This case is tested without the detection of "trouble cell", which shows the robustness of the weighted least square reconstruction to deal with the flow with weak discontinuities.

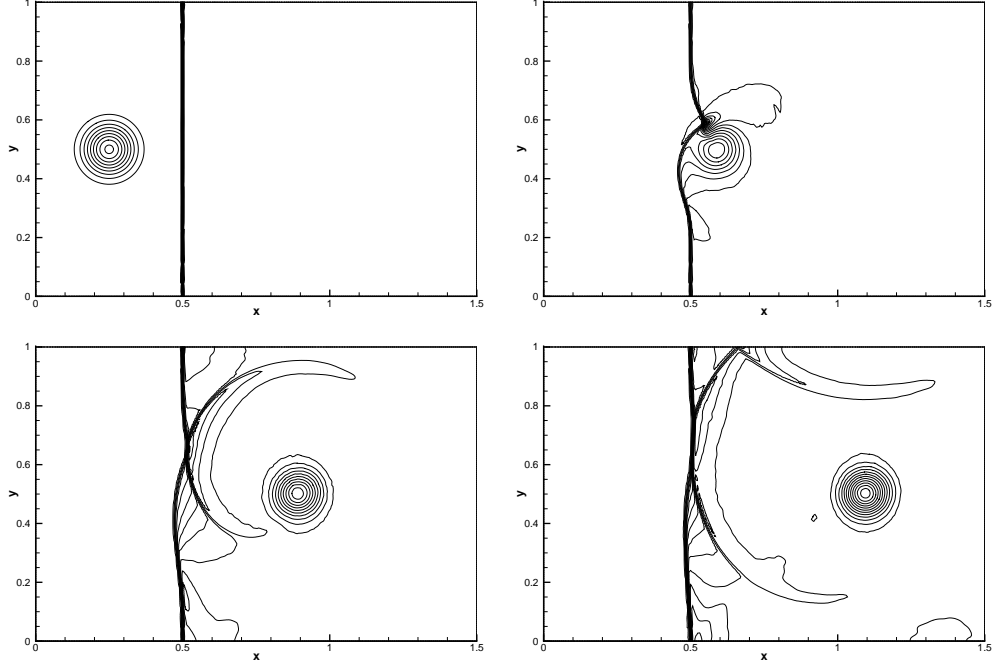


Figure 10: Shock vortex interaction: the pressure distributions at  $t = 0.3$  and  $0.8$  with mesh size  $h = 1/150$ .

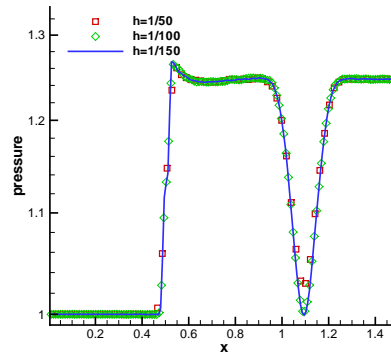


Figure 11: Shock vortex interaction: the pressure distribution at  $t = 0.8$  along the horizontal symmetric line  $y = 0.5$  with mesh size  $h = 1/50, 1/100$  and  $1/150$ .

#### 4.5. Double Mach reflection problem

This problem was extensively studied by Woodward and Colella for the inviscid flow [22]. A shock moves down in a tube which contains a  $30^\circ$  wedge. The computational domain is shown in Fig.15 with mesh size  $h = 1/20$ . The shock wave has a strength with Mach number 10, which is initially positioned at  $x = 0$ . The initial pre-shock and post-shock conditions are

$$\begin{aligned}(\rho, u, v, p) &= (8, 8.25, 0, 116.5), \\(\rho, u, v, p) &= (1.4, 0, 0, 1).\end{aligned}$$

The reflective boundary conditions are used along the wedge, while for the rest of bottom boundary, the exact post-shock condition is imposed. At the top boundary, the flow variables are set to describe the exact motion of the shock front along the wall. The inflow and outflow boundary conditions are used at the entrance and the exit. In this case, the weighted least square reconstruction is not enough, and the shock detection technique is used to switch to the second-order initial reconstruction. The density distributions with mesh size  $h = 1/240$  and  $1/360$  at  $t = 0.2$  are shown in Fig.13. The compact scheme resolves the flow structure under the triple Mach stem clearly.

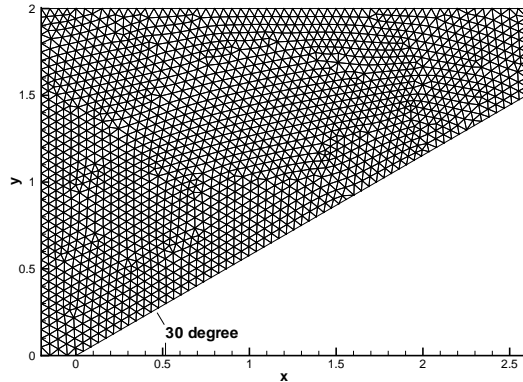


Figure 12: Double Mach reflection: computational domain with mesh size  $h = 1/20$ .

#### 4.6. Mach step problem

The Mach step problem was again studied extensively by Woodward and Colella [22] for the inviscid flow. The computational domain  $[0, 3] \times [0, 1]$  is shown in Fig.15, which is covered by unstructured mesh with mesh size  $h = 1/20$ . The Mach step is located at  $x = 0.6$  with height 0.2 in the tunnel. Initially, a right-moving flow with Mach 3 is imposed in the whole computational domain. The reflective boundary conditions are used along the walls of the tunnel, and inflow and outflow boundary conditions are used at the entrance and the exit. The corner of the step is the center of a rarefaction fan, which is a singularity point. To minimize the numerical error generated at the corner, the meshes near the corner are refined, shown in Fig.15. In this case, the weighted least square reconstruction is not enough, and

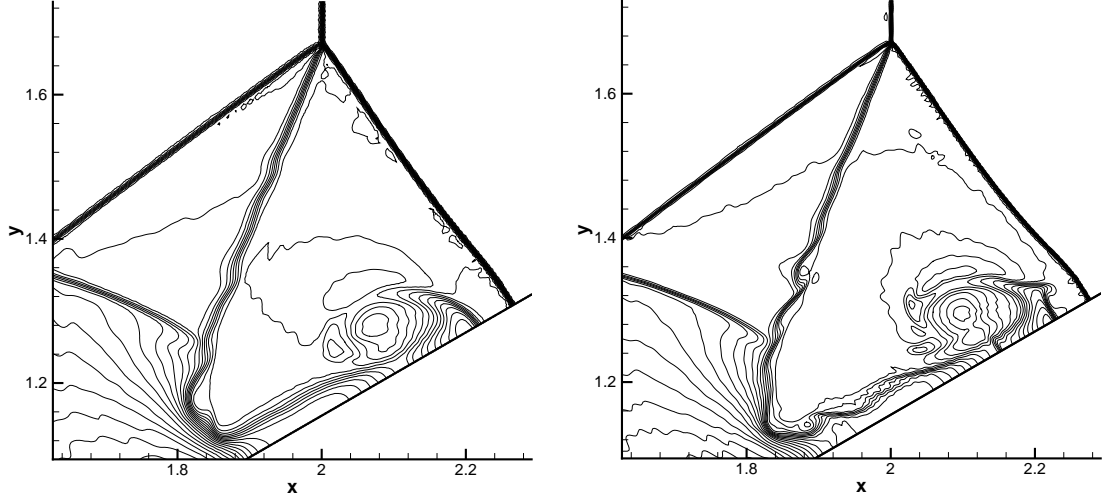


Figure 13: Double Mach reflection: density contours with the mesh size  $1/240$ , and  $1/360$ .

the shock detection technique is used again to switch to the second-order reconstruction. The density distributions with  $h = 1/60, 1/120$ , and  $1/240$  at  $t = 4$  are presented in Fig.15. With the mesh refinement, the resolution is improved, especially for the slip line started from the triple point.

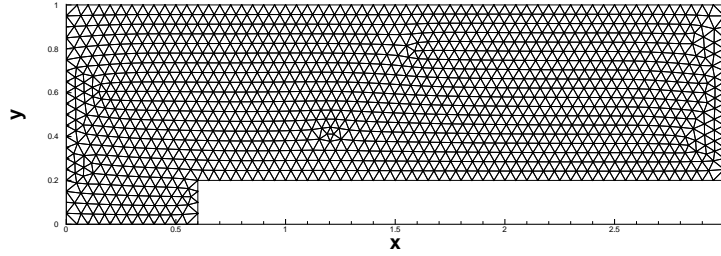


Figure 14: Mach step problem: the computational domain with mesh size  $h = 1/20$ .

#### 4.7. Lid-driven cavity flow

The lid-driven cavity problem is one of the most important benchmarks for validating incompressible or low speed Navier-Stokes flow solvers. The fluid is bounded by a unit square and driven by a uniform translation of the top boundary. In this case, the gas has a specific heat ratio  $\gamma = 5/3$  and the up wall is moving with a speed of Mach number  $Ma = 0.15$ . Isothermal and nonslip boundary conditions are imposed. The computational domain  $[0, 1] \times [0, 1]$  with unstructured mesh is presented in Fig.16, where mesh size are  $h = 1/25$  for the inner cells and  $h = 1/50$  near the walls. Numerical simulations are conducted for three Reynolds numbers  $Re = 400, 1000$  and  $3200$ . The streamlines with  $Re = 1000$  for the compact scheme are shown in Fig.16. The results of  $U$ -velocities along the center vertical line,  $V$ -velocities along the center horizontal line, and the benchmark

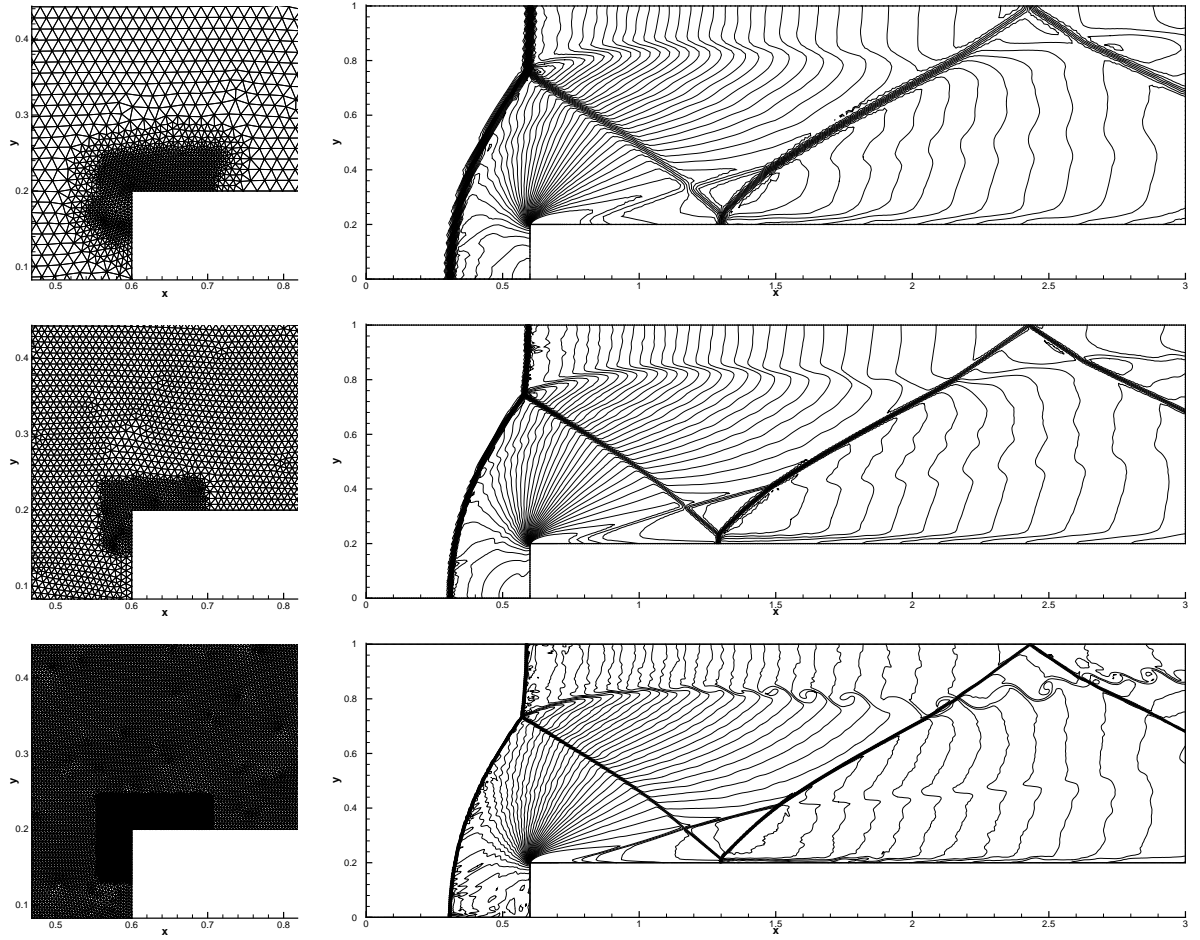


Figure 15: Mach step problem: density contours with the mesh size  $h = 1/60, 1/120$ , and  $1/240$ .

data [8] are shown in Fig.17 for  $Re = 400, 1000, 3200$ . The simulation results match well with the benchmark data.

#### 4.8. Laminar boundary layer

A laminar boundary layer is tested over a flat plate with length  $L = 100$ . The Mach number of the free-stream is  $Ma = 0.15$  and the Reynolds number is  $Re = U_\infty L / \nu = 10^5$ ,  $\nu$  is the viscous coefficient. This case is tested with the compact scheme for the both triangle mesh and rectangular mesh. Fig.18 presents both triangular and rectangular meshes, with an enlarged view of meshes near the boundary. The non-slip adiabatic boundary condition at the plate is used and a symmetry condition is imposed at the bottom boundary before the flat plate. The non-reflecting boundary condition based on the Riemann invariants is adopted for the other boundaries. The non-dimensional velocity  $U$  and  $V$  at different locations are given in Fig.19 for the triangular mesh and Fig.20 for the rectangular mesh. In all locations, the numerical solutions match with the exact Blasius solutions very well. Here the boundary layer can be resolved by six or seven mesh points. The solutions show the

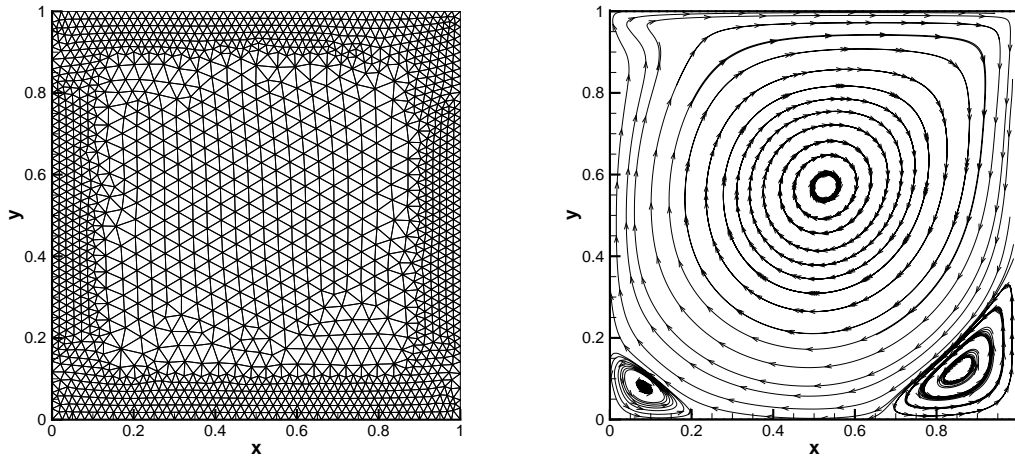


Figure 16: Lid-driven cavity flow: mesh and streamlines for the compact gas-kinetic scheme with  $Re = 1000$ .

good performance of the compact scheme for the Navier-Stokes solutions with unstructured mesh.

#### 4.9. Viscous shock tube problem

This problem was introduced in [5] to test the performances of different schemes for viscous flows. In this case, an ideal gas is at rest in a two-dimensional unit box  $[0, 1] \times [0, 1]$ . A membrane located at  $x = 0.5$  separates two different states of the gas and the dimensionless initial states are

$$(\rho, u, p) = \begin{cases} (120, 0, 120/\gamma), & 0 < x < 0.5, \\ (1.2, 0, 1.2/\gamma), & 0.5 < x < 1, \end{cases}$$

where  $Re = 200$  and Prandtl number  $Pr = 0.73$ .

Scheme	AUSMPW+	M-AUSMPW+	WENO-GKS	triangular	rectangular
height	0.163	0.168	0.165	0.164	0.166

Table 2: Comparison of the height of primary vortex between gas kinetic schemes and reference data [12] for the reflected shock-boundary layer interaction.

The membrane is removed at time zero and wave interaction occurs. A shock wave, followed by a contact discontinuity, moves to the right with a Mach number  $Ma = 2.37$ , and reflects at the right end wall. After the reflection, it interacts with the contact discontinuity. The contact discontinuity and shock wave also interact with the horizontal wall and create a thin boundary layer during their propagation. The solution will develop complex two-dimensional shock/shear/boundary-layer interactions. This case is tested in the computational domain  $[0, 1] \times [0, 0.5]$ . A symmetrical condition is used on the top boundary



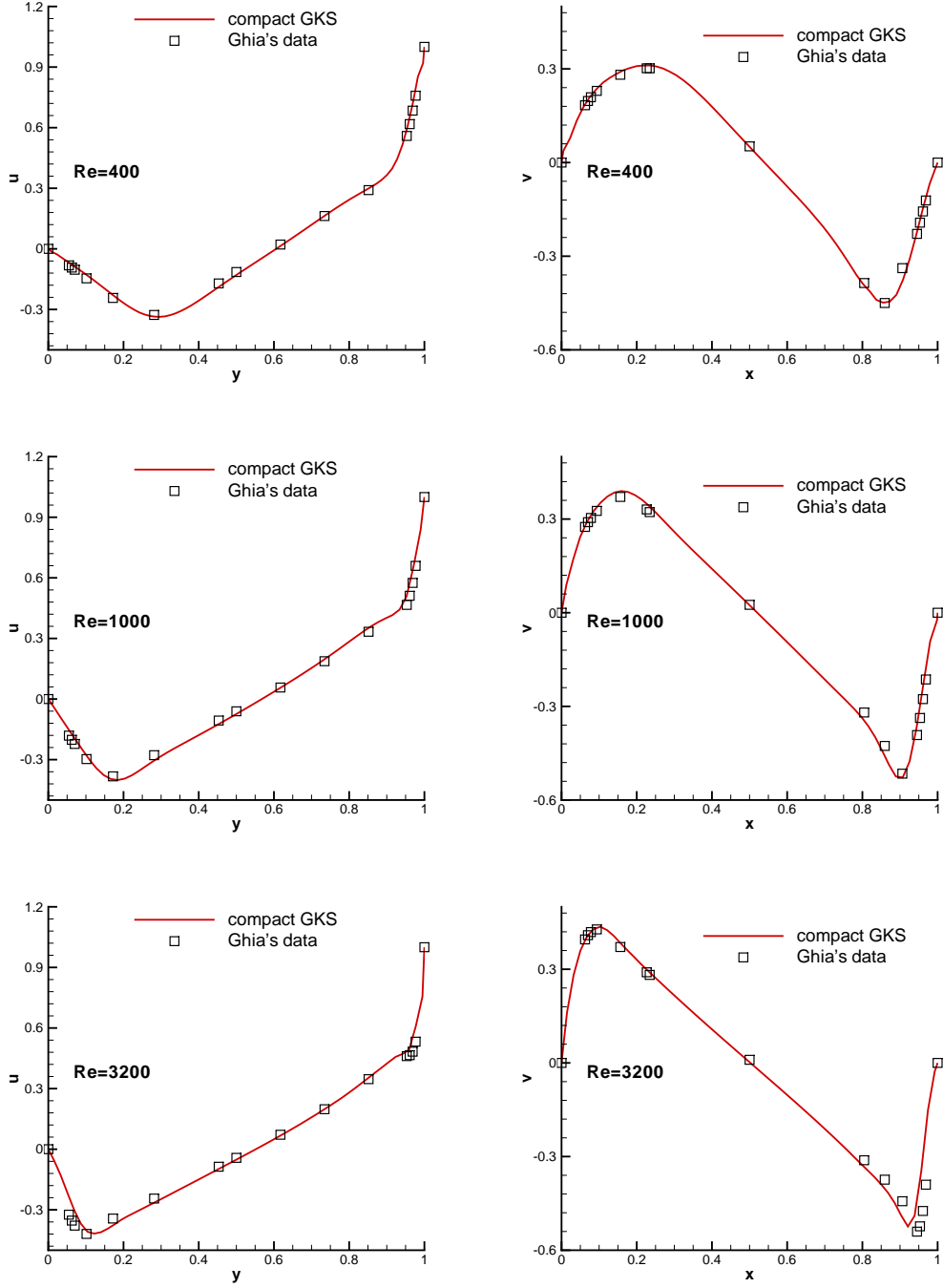


Figure 17: Lid-driven cavity flow:  $U$ -velocities along vertical centerline line and  $V$ -velocities along horizontal centerline with  $Re = 400, 1000$  and  $3200$ . The reference data is from Ghia [8].

$x \in [0, 1]$ ,  $y = 0.5$ , and non-slip boundary condition and adiabatic condition for temperature are imposed at solid wall boundaries. The density distributions for the compact scheme

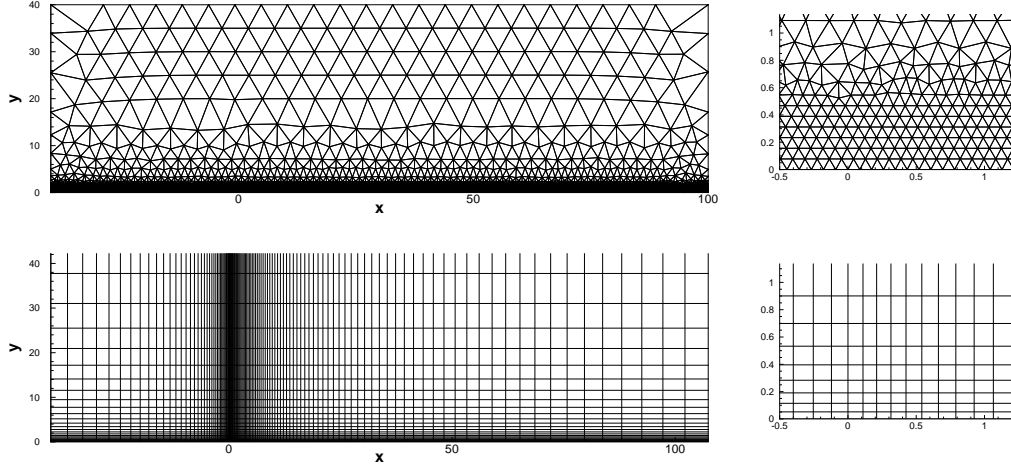


Figure 18: Laminar boundary layer computation: the triangular and rectangular meshes.

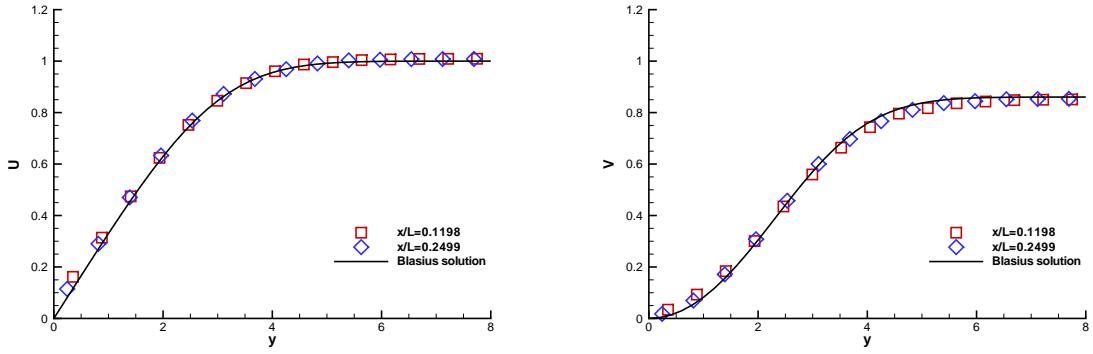


Figure 19: Laminar boundary layer solution from compact scheme with triangular mesh: the non-dimensional velocity  $U$  and  $V$ .

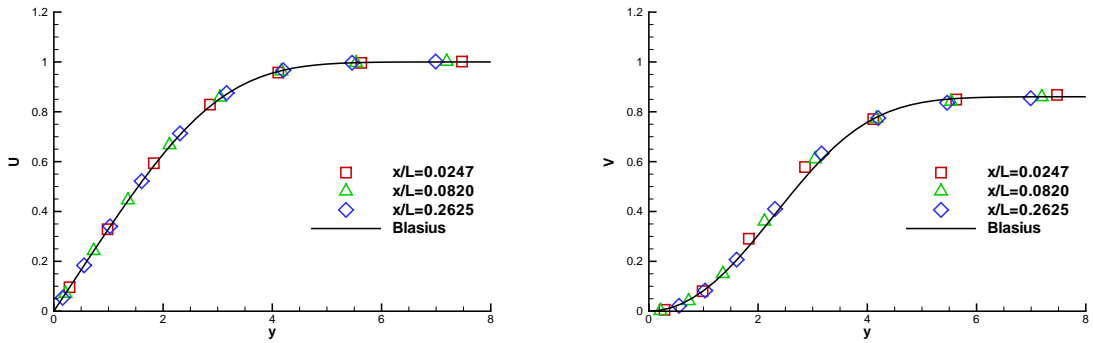


Figure 20: Laminar boundary layer solution from compact scheme with rectangular mesh: the non-dimensional velocity  $U$  and  $V$ .



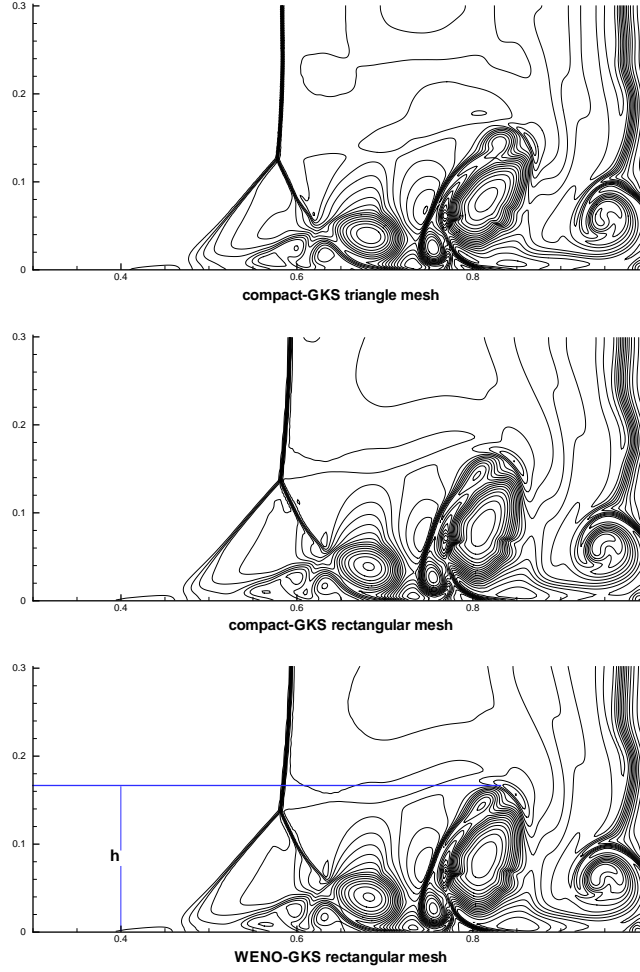


Figure 21: Reflected shock-boundary layer interaction: the density distribution at  $t = 1$  with  $Re = 200$ .

with the rectangular mesh with mesh size  $\Delta x = \Delta y = 1/500$  and the triangular mesh with mesh size  $h = 1/500$  are given in Fig.21. As a reference, the density distribution of the WENO-GKS with a structured mesh size  $\Delta x = \Delta y = 1/500$  is also presented [17]. The current scheme can resolve the complex flow structure. As shown in Table.2, the height of primary vortex predicted by the current scheme agrees well with the reference data [12]. and the GKS-WENO results with the same structure mesh.

## 5. Conclusion

In this paper, a third-order compact gas-kinetic scheme is proposed on unstructured mesh for both inviscid and viscous flow simulations. The merit of the gas-kinetic scheme is that due to a higher-order gas evolution model the time-dependent solution of gas distribution at a cell interface can provides both numerical fluxes and the point-wise flow variables. Therefore, the scheme can be designed in a compact way, where both the cell averaged and

cell interface flow variables can be used for the initial data reconstruction at the beginning of next time level. With the inclusion of neighboring cells only, a compact third-order gas-kinetic scheme is constructed, where the weighted least-square method is used for the data reconstruction on the unstructured mesh. In comparison with former compact gas-kinetic scheme, the use of least-square procedure avoids the difficulty in choosing different stencils. The systematic way of including all weighted stencils makes the compact reconstruction suitable for different kind of meshes. Different from other higher-order schemes based on the Riemann solution, the current method avoids the use of Gaussian points integration for the flux transport along a cell interface and the multi-stage Runge-Kutta time stepping technique. The compact scheme has been tested from smooth viscous flow to the cases with strong discontinuities. The numerical results confirm the accuracy and robustness of the current third-order compact scheme.

## Acknowledgement

The work was supported by Hong Kong research grant council (620813, 16211014, 16207715).

## References

- [1] R. Abgrall On essentially non-oscillatory schemes on unstructured meshes: analysis and implementation. *J. Comput. Phys.* 144 (1994) 45-58.
- [2] T.J. Barth, P.O. Frederickson, Higher order solution of the Euler equations on unstructured grids using quadratic reconstruction. *AIAA* (1990) 90-0013.
- [3] P.L. Bhatnagar, E.P. Gross, M. Krook, A Model for Collision Processes in Gases I: Small Amplitude Processes in Charged and Neutral One-Component Systems, *Phys. Rev.* 94 (1954) 511-525.
- [4] S. Chapman, T.G. Cowling, *The Mathematical theory of Non-Uniform Gases*, third edition, Cambridge University Press, (1990).
- [5] V. Daru, C. Tenaud, High order one-step monotonicity-preserving schemes for unsteady compressible flow calculations, *J. Comput. Phys.* 193 (2004) 563-594.
- [6] M. Dumbser, M. Käser, V.A. Titarev, E.F. Toro. Quadrature-free non-oscillatory finite volume schemes on unstructured meshes for nonlinear hyperbolic systems, *J. Comput. Phys.* 226 (2007), 204-243.
- [7] O. Friedrich, Weighted essentially non-oscillatory schemes for the interpolation of mean values on unstructured grids, *J. Comput. Phys.* 144 (1998) 194-212.
- [8] U. Ghia, K. N. Ghia, C.T Shin, High-Re solutions for incompressible flow using the Navier-Stokes equations and a multigrid method, *J. Comput. Phys.* 48 (1982) 387-411.
- [9] Z.L. Guo, K. Xu, R.J. Wang, Discrete unified gas kinetic scheme for all Knudsen number flows: Low-speed isothermal case, *Physical Review E*, 88 (2013) 033305.
- [10] J. Jiang, Y.H. Qian, Implicit gas-kinetic BGK scheme with multigrid for 3D stationary transonic high-Reynolds number flows, *Computers & Fluids*. 66 (2012) 21-28.
- [11] G.S. Jiang, C. W. Shu, Efficient implementation of Weighted ENO schemes, *J. Comput. Phys.* 126 (1996) 202-228.
- [12] K.H. Kim, C. Kim, Accurate, efficient and monotonic numerical methods for multi-dimensional compressible flows Part I: Spatial discretization, *J. Comput. Phys.* 208 (2005) 527-569.
- [13] L. Krivodonova, J. Xin, J.F. Remacle, N. Chevaugeond, J.E. Flaherty, Shock detection and limiting with discontinuous Galerkin methods for hyperbolic conservation laws, *Applied Numerical Mathematics* 48 (2004) 323-338.

- [14] G. Kumar, S.S. Girimaji, J. Kerimo, WENO-enhanced gas-kinetic scheme for direct simulations of compressible transition and turbulence, *J. Comput. Phys.* 234 (2013) 499-523.
- [15] Q. Li, K. Xu, S. Fu, A high-order gas-kinetic Navier-Stokes flow solver, *J. Comput. Phys.* 229 (2010) 6715-6731.
- [16] J. Luo, L.J. Xuan, and K. Xu, Comparison of fifth-order WENO scheme and WENO-gas-kinetic scheme for inviscid and viscous flow simulation, *Commun. Comput. Phys.*, 14 (2013) 599-620.
- [17] J. Luo, K. Xu, A high-order multidimensional gas-kinetic scheme for hydrodynamic equations, *SCIENCE CHINA Technological Sciences*, 56 (2013) 2370-2384.
- [18] L. Mieussens, On the asymptotic preserving property of the unified gas-kinetic scheme for the diffusion limit of linear kinetic models, *J. Comput. Phys.* 253 (2013) 138-156.
- [19] C. F. Ollivier-Gooch Quasi-ENO schemes for unstructured meshes based on unlimited data-dependent least-square reconstruction, *J. Comput. Phys.*, 133 (1997) 6-17.
- [20] L. Pan, K. Xu A compact third-order gas-kinetic scheme for compressible Euler and Navier-Stokes equations, *Commun. Comput. Phys.* 18 (2015) 985-1011.
- [21] M. Pandolfi, and D. D'Ambrosio, Numerical Instabilities in Upwind Methods: Analysis and Cures for the "Carbuncle" Phenomenon, *J. Comput. Phys.* 166 (2001) 271-301.
- [22] P. Woodward, P. Colella, The numerical simulation of two dimensional fluids with strong shock, *J. Comput. Phys.* 54 (1984) 115-173.
- [23] K. Xu, *Direct Modeling for Computational Fluid Dynamics: Construction and Application of Unified Gas-kinetic Schemes*, World Scientific (2015).
- [24] K. Xu, A gas-kinetic BGK scheme for the Navier-Stokes equations and its connection with artificial dissipation and Godunov method, *J. Comput. Phys.* 171 (2001) 289-335.
- [25] K. Xu, J. Huang, A unified gas-kinetic scheme for continuum and rarefied flows, *J. Comput. Phys.* 229 (2010) 7747-7764.